Measurement and modeling of a diamond deposition reactor: Hydrogen atom and electron number densities in an Ar/H_2 arc jet discharge

C. J. Rennick, R. Engeln,[a] J. A. Smith, A. J. Orr-Ewing, and M. N. R. Ashfold[b]
School of Chemistry, University of Bristol, Cantock's Close, Bristol BS8 1TS, United Kingdom

Yu. A. Mankelevich
Nuclear Physics Institute, Moscow State University, 119992 Moscow, Russia

(Received 17 November 2004; accepted 21 March 2005; published online 1 June 2005)

A combination of experiment [optical emission and cavity ring-down spectroscopy (CRDS) of electronically excited H atoms] and two-dimensional (2D) modeling has enabled a uniquely detailed characterization of the key properties of the Ar/H_2 plasma within a $\leqslant$10-kW, twin-nozzle dc arc jet reactor. The modeling provides a detailed description of the initial conditions in the primary torch head and of the subsequent expansion of the plasma into the lower pressure reactor chamber, where it forms a cylindrical plume of activated gas comprising mainly of Ar, Ar^+, H, ArH^+, and free electrons. Subsequent reactions lead to the formation of H_2 and electronically excited atoms, including $H(n=2)$ and $H(n=3)$ that radiate photons, giving the plume its characteristic intense emission. The modeling successfully reproduces the measured spatial distributions of $H(n>1)$ atoms, and their variation with H_2 flow rate, $F^0_{H_2}$. Computed $H(n=2)$ number densities show near-quantitative agreement with CRDS measurements of $H(n=2)$ absorption via the Balmer-β transition, successfully capturing the observed decrease in $H(n=2)$ density with increased $F^0_{H_2}$. Stark broadening of the Balmer-β transition depends upon the *local* electron density in close proximity to the $H(n=2)$ atoms. The modeling reveals that, at low $F^0_{H_2}$, the maxima in the electron and $H(n=2)$ atom distributions occur in different spatial regions of the plume; direct analysis of the Stark broadening of the Balmer-β line would thus lead to an underestimate of the peak electron density. The present study highlights the necessity of careful intercomparisons between quantitative experimental data and model predictions in the development of a numerical treatment of the arc jet plasma. The kinetic scheme used here succeeds in describing many disparate observations—e.g., electron and $H(n=2)$ number densities, spatial distributions of optical emission from the plume, the variation of these quantities with added flow of H_2 and, when CH_4 is added, absolute number densities and temperatures of radicals such as C_2 and CH. The remaining limitations of the model are discussed. © *2005 American Institute of Physics*. [DOI: 10.1063/1.1906288]

I. INTRODUCTION

Plasmas are ubiquitous in the modern world, finding use in such diverse situations as lighting, sterilization, display technology, and surface modification. The latter application usually implies processing to improve the surface properties, which often requires material modification on scales approaching atomic dimensions. This is where the power of a plasma comes into its own; plasmas can be used as a very clean source of radicals and ions, enabling well-defined and controlled chemistry to occur both within the plasma and at the plasma-surface interface—leading to material deposition and/or etching, according to the chosen process conditions.

The number of designs of plasma sources almost matches the variety of applications, but certain overall distinctions can be made. Regardless of the generation method, the plasma is created either at the point of process (e.g., radio frequency (rf) plasma etching as used in semiconductor processing, which is characterized by a high ion density leading the chemistry) or, remotely, as in an arc such as used here, where the plasma is generated in a separate chamber and allowed to expand so as to form a jet. The ion density in the latter plasma type decreases with propagation distance, and neutral molecule and radical-based chemistry generally dominates in any eventual material processing.

Argon and argon/hydrogen plasmas find widespread use in materials processing, and there is now an extensive literature relating to such plasmas—operating under a wide variety of activation regimes.[1–11] The particular application addressed here employs an Ar/H_2 plasma, in the form of a dc arc jet, for methane activation and subsequent chemical vapor deposition (CVD) of polycrystalline diamond.[12–20] For completeness, we note that microwave-activated hydrocarbon/H_2/Ar gas mixtures find even more widespread use for growing both CVD of single crystal,[21] microcrystalline,[22] and (at very low H_2 partial pressures) ultrananocrystalline diamond films.[23]

In this and a subsequent article[24] we present a detailed and comprehensive analysis of the gas-phase chemistry underpinning the growth of polycrystalline diamond in a dc arc jet reactor operating with a $CH_4/H_2/Ar$ mixture, involving

[a]Permanent address: Department of Applied Physics, Eindhoven University of Technology, P.O. Box 513, 5600 MB Eindhoven, The Netherlands.
[b]Author to whom correspondence should be addressed; FAX: +44 117 925 0612; electronic mail: mike.ashfold@bris.ac.uk

both experiment and complementary modeling. The present article focuses on the analysis of the base Ar/H_2 plasma expansion used in the 10-kW twin-torch dc arc jet reactor at the University of Bristol. The experimental investigations involve wavelength and spatially resolved optical emission spectroscopy (OES) of $H(n=3)$ atoms, via their $n=3\rightarrow n=2$ Balmer-α emission, and high-resolution line-of-sight absorption measurements of $H(n=2)$ atoms (via the $n=4\leftarrow n=2$ Balmer-β transition) in the expanding plume. The absorption measurements employ cavity ring-down spectroscopy (CRDS).[25,26] This noninvasive, multipass laser technique allows determination of radially (r) averaged absolute $H(n=2)$ atom column densities and, from measurement of the Stark broadening of the Balmer-β line, estimates of the local electron density, as a function of distance from the nozzle (z) and of process conditions (e.g., input power, gas mixing ratios, pressure).

Aspects of the companion modeling have been reported previously, in rationalizing the measured CH and C_2 radical concentrations during diamond CVD in this same reactor.[19,20] A more complete analysis of carbon cycling in the Ar/H_2 plasma is reserved for a companion publication.[24] The present work presents self-consistent two-dimensional (2D) (r,z) modeling of the Ar/H_2 plasma generation and subsequent plasma chemical transformations and heat and mass transfer processes, as it expands within the arc jet reactor. The simulations reveal the formation of a shock in the supersonic jet, ~6 mm downstream from the nozzle orifice, and predict inhomogeneous spatial distributions of species concentrations within the reaction chamber that are in essentially quantitative accord with the available experimental observations.

The remainder of this article is structured as follows: First, we present a detailed description of the twin-torch dc arc jet reactor and the application of OES and CRDS methods. This is followed by a discussion of energy balance considerations in the plasma torches that, when combined with appropriate theory, enables estimation of the plasma conditions within, and at the exit of, the primary torch. The subsequent expansion of the Ar/H_2 plasma jet is then described in the light of a reduced chemical reaction mechanism, and 2D spatial distributions of key properties (e.g., gas temperature, flows, etc.) and species number densities (of ions, neutrals, and electrons) are presented and compared with available experimental data.

II. EXPERIMENT

The Bristol dc arc jet reactor is used for chemical vapor deposition of thin films of polycrystalline diamond, and its operating parameters have been described briefly elsewhere.[17–20] A thorough description of the system is given here. The reactor consists of a twin plasma torch assembly housed within a vacuum chamber, with the torches and the body of the reactor cooled by circulated chilled water. The vacuum chamber is equipped with several viewports to enable optical emission and laser measurements of the chemical composition of the gas plume. The characterization of the Ar/H_2 plasma jet reported here employed both camera imaging of the spatial distributions of intensity of the light emitted from the plume and laser absorption CRDS. In this section, the arc jet reactor and the optical diagnostics are described in turn.

A. The arc jet reactor

The dc arc jet reactor is constructed from a modified atmospheric plasma-spray torch system (Onoda), with gas expansion into a vacuum chamber, the pressure of which is controlled by a throttled rotary pump (Edwards E2M40). The torch head is of a two-nozzle design, with a primary nozzle through which Ar and an Ar/H_2 mixture are flowed and a secondary nozzle (which conducts a much lower flow of pure Ar) placed 10 mm from, and perpendicular to, the primary nozzle exit. The secondary flow serves to stabilize the plasma and provides a means of control of the diameter of the gas plume. The nozzles are assembled from copper components, and are cooled by parallel flows of high-pressure (9 bar) chilled, deionized, and filtered water. The temperature of this water was monitored in experiments described in the following section to determine the power coupling into the plasma.

The primary (N) torch is of a two-chamber design, as shown in Fig. 1. The discharge is struck in argon as it flows from the first chamber; a short radio-frequency burst between a conical tungsten electrode and the copper body of the nozzle provides the necessary discharge. Argon is introduced at a flow rate of 10 standard liters per minute (slm) and a pressure of 4 bar, with the flow controlled by a gravity flow meter. The Ar plasma expands into an intermediate chamber where H_2 is added (and undergoes rapid thermal dissociation to H atoms), together with additional argon, so as to raise the total flow rate F^0 to 13.2 slm. The entire plasma mixture expands supersonically through a converging/diverging nozzle into the main vacuum chamber. The secondary (P) torch is of a simpler design, having only one chamber. It is fitted with a copper electrode and strikes a discharge in a pure argon flow of 0.75 slm. The combined power consumptions of the two nozzles are $\leqslant$10 kW but, under typical operating conditions, currents drawn are ~80 A with an applied voltage of 80 V.

In contrast to our earlier descriptions of deposition in this reactor, we define the exit of the N-torch nozzle (rather than the substrate surface) as $z=0$. The reactor chamber comprises a series of cylindrical sections, the dimensions of which are indicated in the cross-sectional view displayed in Fig. 1. The internal diameter is always considerably greater than the luminous part of the arc jet gas plume (~15-mm diameter). The molybdenum substrate (26-mm diameter) is mounted on a translatable, water-cooled rod inserted into the vacuum chamber from the opposite side to the torch heads, and coaxially with the gas plume. z translation of this stage is possible, but the front face of the substrate is typically positioned at $z\sim155$ mm. No current is transferred through the plasma to the substrate. The plasma thus behaves like an electrically neutral flame and, in this regard, the dc arc jet thus differs from other arc jet plasma-generation techniques such as plasma-transferred arcs. The annular injection ring

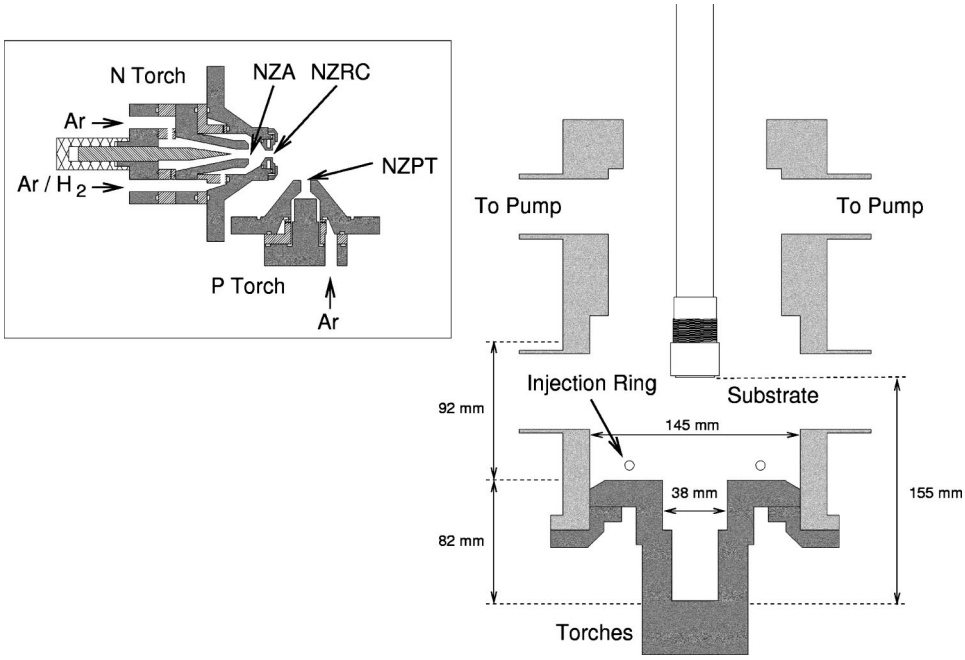

FIG. 1. Cross-sectional schematic diagrams of the torch heads and the arc jet reactor chamber. Labels are defined in the main text. The torch assembly is mounted so that the N torch points towards the center of the substrate holder (i.e., vertically in the main figure).

used for hydrocarbon addition (and thus not used in the present work) is centerd at $z=92.4$ mm and has a radius $r=44.7$ mm.

The pressure within the reactor chamber is typically maintained at 50 Torr, as measured by a capacitance manometer. Two exit ports located on opposite sides of the chamber are attached to the vacuum pumping line to establish stable and symmetric flow conditions.

B. Plume imaging

The highly luminous plasma jet is conveniently monitored by OES. The discharge in Ar/H_2 results in a bright red color characteristic of H atom Balmer-α emission, demonstrating the abundance of electronically excited atoms in the plume. Spatial distributions of this emission were imaged through a quartz window by a monochrome TV camera located vertically above the horizontally propagating plume. The camera images were captured on a personal computer (PC), using a video card for further analysis. Calibrated neutral-density filters were used to bring the brightness within the dynamic range of the camera, and spatial distributions of various atomic emission lines such as H Balmer-α ($\lambda=656.3$ nm) and Balmer-β (486.1 nm) were measured by imaging through appropriate narrow-band interference filters. The inner diameter of the sidearm holding the window flange limits the field of view of the camera to the region $120<z<160$ mm, and a vignetting function was determined by imaging the spatially extensive emission from a (lower pressure) pure Ar plasma.

It proves convenient at this stage to display and describe illustrative images of the H Balmer-α emission, in order to put the subsequent discussion in context. Figure 2 shows four such images, recorded with H_2 input flow rates $F^0_{H_2}=0.2$, 0.5, 1.0, and 1.5 slm, respectively. The emission at the lowest $F^0_{H_2}$ values extends across the entire viewing region and exhibits maximum intensity (due to scattering) at the

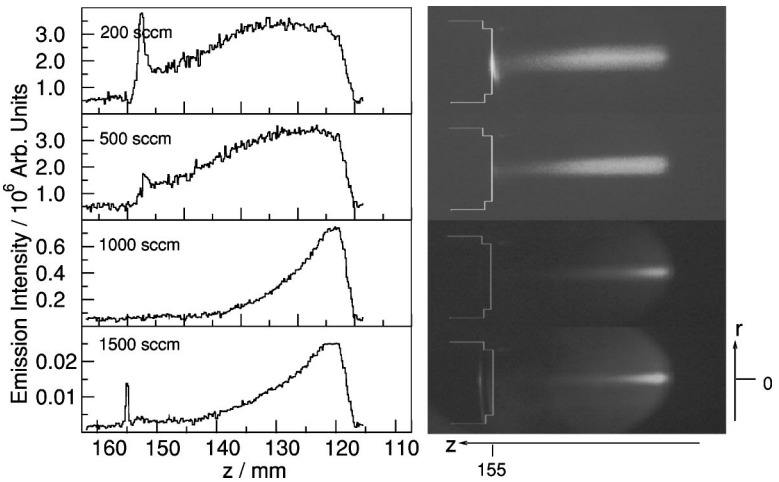

FIG. 2. Optical emission images of the arc jet plume for an Ar/H_2 plasma. The right-hand column shows 2D camera images obtained using an interference filter to transmit only H Balmer-α emission; the images from top to bottom were taken for flow rates of 0.2, 0.5, 1.0, and 1.5 slm of added H_2. Emission was accumulated through neutral-density filters with respective optical densities (OD) of 4.5, 4.5, 3.5, and 2.0, and the contrasts within the images have been arbitrarily scaled for clarity. The left-hand column shows plots of accumulated emission along the central ($r=0$) axis of the plume for the same flow rates as the adjacent images, with intensities corrected for the ODs of the neutral-density filters. The front face of the substrate is at $z=155$ mm.

substrate surface. By eye, the edge of this emission (i.e., at $r>0$) is clearly more intense than the on-axis ($r=0$) emission, implying an annular structure to the Balmer-α emission at low $F^0_{H_2}$. Increasing $F^0_{H_2}$ causes the Balmer-α emission to retreat progressively to smaller z and to concentrate on-axis; the Balmer-α emission intensity in the viewing region falls steeply. We return to consider these trends more quantitatively after discussion of the plasma modeling.

C. Cavity ring-down spectroscopy

CRDS is a sensitive, laser-based absorption spectroscopic technique that relies on measurement of the rate of loss of light from a high-finesse optical cavity as a function of laser wavelength.[25,26] In the current study, CRDS was used to monitor electronically excited H($n=2$) atoms and thereby determine their column densities (number densities integrated along the line of sight of the laser beam) and, from the Stark-broadened lineshapes, the local electron densities. The source of the wavelength-tunable pulsed radiation was a dye laser (Spectra Physics PDL3) pumped by the 355-nm third harmonic of an Nd: yttrium aluminum garnet (YAG) laser (Continuum Surelite III) operating at 10-Hz repetition rate, with laser pulse durations of $\sim$8 ns. The ring-down cavity (RDC) was formed from two high-reflectivity mirrors placed 1.1-m apart, and the laser beam was coupled into the RDC through one cavity mirror using beam-shaping optics. The cavity itself was arranged so that the light propagating between the two mirrors passed through the center of the plasma plume, perpendicular to its propagation direction and at $z=140$ mm. A photomultiplier tube (PMT) was placed behind the rear mirror to monitor light leaking from the RDC, and the transient signal associated with the ring-down of intracavity light intensity was recorded on a digital storage oscilloscope (LeCroy 9361, 8-bit vertical digitization resolution). A narrow bandpass filter, centered at the wavelength of the absorption feature of interest, was placed in front of the PMT to discriminate effectively against broadband emission from the very luminous gas plume. Ring-down decay traces captured by the photomultiplier tube were transferred to a personal computer via a general purpose interface bus (GPIB). Custom-written software was used to fit the resulting exponential decay signals to obtain decay rate constants at each laser wavelength. As described later, these can be transformed into absorption coefficients, and thus absorber number densities. The software performs weighted averaging of the outcomes of several laser shots, with rejection of spurious, rapidly decaying transients that are associated with momentary instabilities in the plasma.

The hydrogen atom Balmer-β line was measured in absorption by scanning the laser wavenumber over the range 20 550–20 580 cm^{-1}, using the fundamental output of the dye laser (operating with Coumarin 480 dye) and mirrors with maximum reflectivity in this region of the visible spectrum. Typical ring-down times in the 1.1-m cavity were 750 ns, corresponding to mirror reflectivities of $R=0.995$. The scan over 30 cm^{-1} is necessary to capture the full Lorentzian lineshape of Balmer-β lines Stark-broadened by the local electric field of the free electrons in the plasma. A similar approach has been used recently to measure electron densities in a laser-ablated lithium plume via Stark broadening of the Li($4d \leftarrow 2p$) transition.[27]

The effects of laser-pulse energy on the Balmer-β absorption were investigated carefully, recognising the potential problems of saturation of the line despite the inefficient coupling of laser intensity into the RDC. The effects of these tests and consequences for measurements are described in a later section.

III. COMPUTER MODEL OF THE ARC JET PLASMA

A sophisticated computer model of the arc jet discharge has been constructed to aid understanding of the complicated physical and chemical processes that are involved. In the current study, we focus on a plasma generated from an Ar/H_2 gas mixture. This is the "base" plasma that underpins our models of diamond-film deposition plasmas, in which a carbon source [typically $\sim$80 sccm (standard cubic centimeter per minute) of methane] is incorporated into the gas flow. In this section we describe the elements of the model, and its performance is then quantitatively tested by comparison with experimental measurements. There are three major components to the computer model: first, the parameters of the dc arc discharge and conditions of the nozzle expansion are established by estimating the gas temperature and its degree of ionization. We then describe how the model incorporates the chemistry of ionic and neutral atoms and molecules, and the variation of the electron density. Finally, the treatment of the gas expansion into vacuum, and formation of a gas plume, are discussed. The combination of these three parts leads to a model that successfully reproduces most of the available experimental observations of the plume structure and chemical composition.

A. Arc jet plasma temperature and ionization fraction

The primary gas flow to the N torch is pure Ar, with a smaller secondary flow of an Ar/H_2 mixture combined in the intermediate chamber of the nozzle structure, as shown in Fig. 1. To begin this discussion it is instructive to consider what would be the maximum possible values of gas temperature T, pressure P, and the degree of ionization $X_e=X_{Ar^+}$ in the immediate vicinity of the arc discharge (i.e., near the nozzle arc (NZA) in Fig. 1) if it was possible to couple all 6500 W of supplied power into the Ar feed. Using the Saha equation, and assuming that the electrons, ions, and atoms are all in thermal equilibrium at a common T, the upper-limit values so derived are $T=14\,300$ K, $P\sim3$ atm, and $X_e=0.22$. The gas velocity through the exit orifice at NZA can then be estimated at $\sim$300 m s^{-1} for the experimental argon flow rate (10 slm) and orifice diameter (3.8 mm). The more important input parameters for modeling the subsequent plasma chemistry, however, are the corresponding quantities for the gas exiting at nozzle-reaction chamber boundary (NZRC), i.e., from the mixing region within the N torch, where the additional H_2/Ar mixture is combined with the argon plasma. To estimate these, we first need to determine the power deposited into the gas discharge. This can be derived as follows: we begin by measuring the temperature rise (and thus power

dissipated) in the cooling water flowing through the N- (and P-) torch heads. The difference between this and the supplied power is taken as the power coupled into the plasma. This power is distributed between the two torch heads; we assume it to be partitioned in direct proportion to the (known) division of the total gas flow between the N and P torches, i.e., ~95% to the N torch. For example, under typical H_2-rich operating conditions appropriate for successful CVD diamond growth[17–20] (i.e., input flow rates, $F^0_{Ar}=11.4$ slm and $F^0_{H_2}=1.8$ slm into the N torch, with a further $F^0_{Ar}=0.75$ slm flow into the P torch) and a total supplied power $W_0=6500$ W, we deduce that a total of ~4800 W is coupled into the plasma, with about 350 W passing through the P torch. The gas temperature and other plasma parameters at NZRC can then be estimated from the known total mass flow and the measurements of the variation of the energy injected into the plasma as a function of Ar/H_2 mixing ratio, which depends upon the heat capacity of the plasma and the degree of ionization of the constituents, as described below.

In developing this model we make a further assumption—that only Ar is ionized in the N torch. The justification for this simplification relies on the facts that (i) H_2 will be completely dissociated at the extreme gas temperatures prevailing in this region and (ii) the residence times for H atoms in the hottest core region of the plasma stream ($\sim 3\times10^{-5}$ s) are too short for significant amounts of ionization through collisions with electrons. [We estimate a characteristic time $\tau\sim 1\times10^{-4}$ s for H atom ionization in an equilibrated Ar/H_2 plasma at $T\sim 13\,000$ K and $P\sim 3$ atm from the expression $\tau=(k_I N_e)^{-1}$ and realistic values for the ionization rate ($k_I\sim 3.7\times10^{-14}$ cm^3 s^{-1}) and electron density ($N_e\sim 2.5\times10^{17}$ cm^{-3}). All other collision-induced H atom ionization processes involving species other than electrons in this environment are estimated to be several orders of magnitude less efficient.] We thus proceed with the assumption that the gas mixture in the throat of the nozzle (i.e., at NZRC) is simply composed of Ar, Ar^+, H, and free electrons. The power W in the gas flow is

$$W=\tfrac{3}{2}NkT(X_e+X_{Ar}+X_{Ar^+}+X_H)F+\tfrac{1}{2}NX_HFD_0(H_2)+I_{Ar}NX_{Ar^+}F, \quad (1)$$

where N is the total particle number density, and the various X_i are the mole fractions of species i (=H, Ar, Ar^+, or e), which sum to unity, and F is the flow rate (in units of cm^3 s^{-1}). $\frac{1}{2}D_0(H_2)$ in Eq. (1) gives the heat of formation of an H atom in terms of the bond dissociation energy of H_2 (complete dissociation of H_2 is implicit), and I_{Ar} is the ionization energy of argon. Equation (1) thus establishes a relationship between W and T, but requires knowledge of the various X_i and the overall number density, N.

The flow rate, F, at NZRC can be related to the input flows of H_2 and Ar, $F^0_{H_2}$ and F^0_{Ar} (specified in cm^3 s^{-1} at STP), via

$$F[\text{cm}^3\,\text{s}^{-1}]=\frac{(2F^0_{H_2}+F^0_{Ar})}{(1-X_e)}\frac{N^0}{N}, \quad (2)$$

where N^0 is the number density at STP. Particle balance at NZRC for hydrogen, and for argon, give, respectively: $FNX_H=2F^0_{H_2}N^0$ and $FNX_{Ar}+FNX_{Ar^+}=F^0_{Ar}N^0$. For charge neutrality, X_{Ar^+} and X_e must be equal. X_e can be determined at any temperature by the Saha equation

$$\frac{X_e^2}{1-2X_e-X_H}N=2\frac{g_{Ar^+}}{g_{Ar}}\left(\frac{2\pi m_e kT}{h^2}\right)^{3/2}\exp\left(-\frac{I_{Ar}}{kT}\right), \quad (3)$$

where g_{Ar^+} and g_{Ar} are the degeneracies of the argon ion and atom, respectively. Thus we can derive the individual mole fractions, e.g. $X_H=2F^0_{H_2}N^0/FN$.

We use mass balance arguments to establish a value of the total number density N at NZRC, from which the various number densities of Ar, Ar^+, H, and electrons can be derived using $N_i=X_iN$. The total mass flow rate (F_{mass}) into the reactor is controlled by the mass flow controllers as given by Eq. (4)

$$F_{mass}[\text{g}\,\text{s}^{-1}]=N^0(m_{H_2}F^0_{H_2}+m_{Ar}F^0_{Ar}). \quad (4)$$

By way of illustration, $F_{mass}=0.34$ g s^{-1} for the highest H_2 flow rates used here ($F^0_{H_2}=1.8$ slm, $F^0_{Ar}=11.4$ slm). However, F_{mass} can also be estimated by Eq. (4a), which assumes that gas flow out of the nozzle chamber is well described by a mean gas flow velocity v through a cross-sectional area S'

$$F_{mass}[\text{g}\,\text{s}^{-1}]=S'v\rho, \quad (4a)$$

with ρ as the gas density. The best choice of value for S' is smaller than the physically measured cross-sectional area of the orifice, S, because of edge effects on the gas flow; boundary layer theory[28] suggests a ratio of $S'/S\sim 0.85$. The assumption of a single v (i.e., plug rather than steady-state laminar flow) is dictated by the short length of the nozzle orifice. At the most constricted part of the nozzle, the flow velocity must be equal to the local speed of sound v_s and this in turn can be calculated from the heat capacity ratio $\gamma=C_P/C_\nu=5/3$ for monatomic species via $v_s=\sqrt{\gamma P/\rho}$. It then follows that

$$N=\frac{N^0(m_{H_2}F^0_{H_2}+m_{Ar}F^0_{Ar})}{S'\sqrt{\gamma kT}\sqrt{m_HX_H+m_{Ar}(X_{Ar}+X_{Ar^+})}}, \quad (5)$$

from which N, and hence the N_i, can be deduced from the experimental flow rate.

Equation (1) can thus be used to calculate the powers deposited into the gas mixture as a function of H_2 flow rate (for constant overall flow rate) at a range of temperatures. Representative data are shown in Fig. 3. Temperature affects the power contained in the gas flow. Comparison of the measured variation of the input power to the plasma with H_2 gas flow (while maintaining the total flow rate constant), as shown by the data in Fig. 3, thus determines the temperature of the gas in the throat of the nozzle to be ~12 000–12 100 K for all $F^0_{H_2}>0.4$ slm. As Fig. 3 shows, the gas temperature in the throat of the nozzle (and, most probably, in the intermediate chamber also) is higher at lower

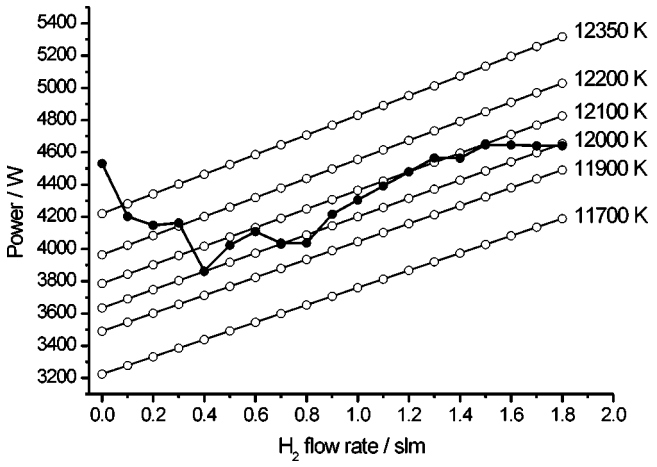

FIG. 3. The diagonal lines connecting open circles show calculated variations of the required power coupled into the plasma within the N-torch and P-torch head for a range of H_2 flows to establish the specified gas temperatures at the nozzle orifice, NZRC. The connected black circles show the experimentally measured power coupled into the plasma (as determined by calorimetric measurements of the power lost to the water flow cooling the torches), from which a gas temperature of 12 100 K is deduced. Argon flow rates were $F^0_{Ar}=13.5-F^0_{H_2}$ [slm] and 0.75 slm in the N and P torches, respectively.

$F^0_{H_2}$. This may be explained by recognizing that the thermal conductivity of H_2 is an order of magnitude higher than that of Ar. Measurements of the power dissipation into the cooling water (Fig. 3) indicate that the total thermal conduction flux on to the intermediate chamber walls (together with any radiation from excited hydrogen atoms) increases with hydrogen input flow rate up to $F^0_{H_2}\sim 0.4$ slm, saturates at $F^0_{H_2}\sim 0.4-0.8$ slm and then decreases as $F^0_{H_2}$ is increased further. The observed decline in power dissipation into the cooling water at higher $F^0_{H_2}$is indicative of the redistribution of input power: as $F^0_{H_2}$ increases, more of the input power is expended on H_2 dissociation and heat transfer to the walls decreases notwithstanding the increase in thermal conductivity that accompanies an increase in $F^0_{H_2}$.

The foregoing analysis allows a rather detailed specification of the conditions prevailing at NZRC. For example, under the previously defined H_2-rich operating conditions, such as are favored for CVD diamond-growth conditions[17–20] (i.e., $F^0_{Ar}=11.4$ slm and $F^0_{H_2}=1.8$ slm flowing into the N torch, with a further $F^0_{Ar}=0.75$ slm into the P torch) and a total power $W=4450$ W coupled into the N-torch plasma, we find $T=12\,100$ K and $P=914$ Torr at NZRC. The gas velocity at the throat of this nozzle, where the cross-sectional diameter is 2.5 mm, will be $\sim 2450\ \mathrm{m\,s^{-1}}$. The foregoing analysis also gives insight into the utilization of this input power: ionization, the last term in Eq. (1), is the dominant sink of this power (consuming ~2100 W and causing a degree of ionization $X_e=0.1$). H_2 dissociation accounts for ~670 W, and the balance is partitioned into the thermal energy of the constituent particles. We note that our earlier, preliminary analyses[20] of power utilization within the plasma focused entirely on thermal excitation mechanisms. Neglect of ionization resulted in underestimation of the heat capacity of the gas, and thus the plasma temperature.

Having established the plasma conditions at NZRC we are now ready to treat the subsequent expansion into the large reactor chamber using a set of conservation equations for mass, momentum, energy, and species concentrations. This requires a model of the relevant chemical kinetics, which we now describe.

B. Plasma chemical model

The chemical processes for both charged and neutral species used to model the composition of the plasma jet are summarized in Table I with their associated kinetic parameters. The processes of greatest significance for the chemical composition of the plume are discussed here.

Electron recombination with Ar^+ ions is stabilized by a third body, most likely to be an electron, because stabilization by Ar atoms is seven to eight orders of magnitude less efficient.[29] The recombination forms highly excited atoms, Ar^{**}, with energies E^{**} lying within a range of the ionization limit approximately corresponding to the thermal energies of the free electrons

$$Ar^+ + e + e \leftrightarrow Ar^{**} + e. \tag{6}$$

Ar^{**} atoms can relax by collisional or radiative mechanisms, with eventual cascade via Ar^* atoms with smaller amounts of internal energy, to ground state Ar atoms [processes (7)–(9)]

$$Ar^{**} + e \leftrightarrow Ar^* + e, \tag{7}$$

$$Ar^{**} \rightarrow Ar^* + h\nu, \tag{8}$$

$$Ar^* \rightarrow Ar + h\nu. \tag{9}$$

Note that process (7) releases energy as heat, whereas radiative decay allows energy to escape from the plasma. The rate coefficient for radiative decay from the lowest Ar^* resonance levels [step (9) with excitation energies of the order of $E^*\sim 11.7$ eV] is approximated by $k_9=\theta_9\times A_9$, where $A_9\sim 3\times 10^8\ \mathrm{s^{-1}}$ is the Einstein A-coefficient for spontaneous emission[30] and θ_9 is an escape factor for the radiation from the plasma. This factor allows for the possibility of resonant reabsorption of this radiation by abundant ground-state Ar atoms.

Electronically excited H atoms can also undergo spontaneous emission and radiative relaxation, illustrated here for $n=2$ atoms because of their significance in experimental measurements discussed later. Ground-state hydrogen atoms, $H(n=1)$ are denoted simply by H.

$$H(n=2) \rightarrow H + h\nu. \tag{10}$$

This process occurs with a rate constant $k_{10}=\theta_{10}\times A_{10}$, with $A_{10}\sim 6.2\times 10^8\ \mathrm{s^{-1}}$ and θ_{10} is, again, a radiation escape factor (which depends upon the H_2 flow). For the highly nonuniform distribution of densities of absorbing species expected in the arc jet plume, the approach used here, with incorporation of escape factors, is approximate and should thus be considered as a relatively crude description of reabsorption effects.

$H(n=2)$ is produced by reaction of H_2 with Ar^+, followed by dissociative recombination of an electron to ArH^+

TABLE I. The kinetic scheme employed in the model. Rate constants are calculated using $k=AT^n \exp(-E_A/RT)$, with the following units: cal, mol, K, cm, and s.

Reactions	A	n	E_A	Reference
$H(3)\rightarrow H(2)+h\nu$	4.4×10^{7}	0	0	44
$H(2)\rightarrow H+h\nu$[a] (Eq. 10)	6.2×10^{8}	0	0	44
$Ar^{+}+e\rightarrow Ar+h\nu$	1.0×10^{13}	−0.5	0	30
$Ar^{+}+e+e\rightarrow Ar+e$[b]	2.46×10^{25}	−1.5	0	See text
$Ar^{+}+e+e\rightarrow Ar+e$[c]	0.54×10^{25}	−1.5	0	See text
$Ar^{+}+e+e\rightarrow Ar+e$[d]	2.47×10^{21}	−1	0	30
$H+H+H_2\rightarrow H_2+H_2$	9.0×10^{16}	−0.6	0	37
$H+H+H\rightarrow H_2+H$	1.0×10^{18}	−1	0	37
$H+H+Ar\rightarrow H_2+Ar$	6.3×10^{17}	−1	0	37
$H(2)+e\rightarrow H(3)+e$	2.0×10^{15}	0.03	4.38×10^{4}	Estimation
$H(3)+e\rightarrow H(2)+e$	6.0×10^{14}	0.08	0	Estimation
$H+e\rightarrow H(2)+e$	3.85×10^{15}	0.11	2.37×10^{5}	[e]
$H(2)+e\rightarrow H+e$	1.45×10^{15}	0.08	2.90×10^{3}	[e]
$H(2)+H_2\rightarrow H+H+H$	7.2×10^{10}	0	0	46
$H(3)+H_2\rightarrow H+H+H$	1.1×10^{11}	0	0	47
$H(2)+Ar\rightarrow ArH^{+}+e$	1.0×10^{13}	0	1.61×10^{4}	Estimation
$H(3)+Ar\rightarrow ArH^{+}+e$	1.0×10^{13}	0	0	Estimation
$Ar^{+}+H_2\rightarrow ArH^{+}+H$ (Eq. 11)	2.36×10^{14}	0.14	0	48
$ArH^{+}+e\rightarrow Ar+H(2)$ (Eq. 12)	1.0×10^{19}	−0.67	0	49
$ArH^{+}+e\rightarrow Ar+H(3)$	1.0×10^{19}	−0.67	2.78×10^{4}	Estimation

[a]The radiation escape factor depends upon the H_2 flow rate and is not included here.
[b]Stabilization of Ar by radiative loss of energy.
[c]Stabilization of Ar by thermal loss of energy.
[d]Three-body recombination directly to ground-state Ar.
[e]The rate coefficient is calculated using cross sections from Physical Encyclopaedia (Moscow, 1988), Vol. 1, p. 300. The reverse reaction rate is obtained from detailed balance.

$$Ar^{+} + H_2 \rightarrow ArH^{+} + H, \tag{11}$$

$$ArH^{+} + e \leftrightarrow Ar + H(n=2). \tag{12}$$

The mechanism also allows for formation of $H(n>2)$, denoted in Table I as $H(n=3)$, by equivalent processes to (12), and subsequent radiative decay forms $H(n=2)$. The primary source of the H_2 for (11) is the gas-phase recombination of two H atoms, stabilized by a third body. Although there is likely to be some additional, small amount of recombination of H atoms on the copper walls of the nozzle, or on the reactor walls,[3,31] these processes are of only minor importance in our model.

Other neutralization channels for Ar^{+} prove to be much less significant, but are nevertheless incorporated in the mechanism (with kinetic data in Table I), although relevant equations are not numbered here. These minor channels include recombination of Ar^{+} with an electron to form ground-state Ar atoms directly

$$Ar^{+} + e + e \rightarrow Ar + e.$$

Radiative recombination to form ground-state Ar,

$$Ar^{+} + e \leftrightarrow Ar + h\nu,$$

is expected to be insignificant because of the rapid reabsorption of emitted photons (i.e., the rate coefficient for this process listed in Table I would need to be reduced by $>2-3$ orders of magnitude because of radiation trapping in the plasma).

Deexcitation of electronically excited Ar atoms by electron collisions,

$$Ar^{*} + e \rightarrow Ar + e,$$

is slower (by about three to four orders of magnitude at the likely electron densities, N_e) than radiative decay by process (9).

In an expanded plasma of the type used in the current study, the temperature drops faster than the ionization degree in the expansion, and thus there is no true equilibration, but we can assume equilibrium between Ar^{+}, electrons, and Ar^{**} (with respective degeneracies $g_{Ar^{+}}$ and $g_{Ar^{**}}$) and describe the relationships between their concentrations using a Saha formulation

$$[Ar^{**}] = [e][Ar^{+}]/f \text{ with } f = \frac{g_{Ar^{+}}}{g_{Ar^{**}}}\left(\frac{2\pi m_e k}{h^2}\right)^{3/2} T^{1.5} \times \exp(-(I_{Ar} - E^{**})/kT). \tag{13}$$

The main radiative energy losses from the plasma occur via processes such as (9) and (10), and from reactions (6)–(9) and Eq. (13) we have

$$k_4[Ar^{*}] = [e]^2[Ar^{+}]\left(k_7 + \frac{k_8}{[e]}\right)\frac{1}{f} \approx [e]^2[Ar^{+}]\frac{C}{T^{1.5}}, \tag{14}$$

where k_7 and k_8 are the rate coefficients for (7) and (8), and the coefficient C is taken as a constant. Overall relaxation processes can thus be described by the net process described by scheme (15) that condenses several mechanistic steps into one

$$Ar^+ + e + e \leftrightarrow Ar + e + h\nu, \tag{15}$$

with $k_{15}=C/T^{1.5}$. The only practical method to find either the effective rate coefficient k_{15} or, equivalently, the constant C and the radiation escape factor for (10) is to fit simultaneously all available experimental data, i.e., for H atom Balmer-α optical emission as a function of z and of $F^0_{H_2}$; H($n=2$) column densities and local electron densities described later; as well as previously reported[18–20] column densities and rotational temperatures of carbon-containing radicals such as CH and C_2 that form when CH_4 is added to the gas flow (both in experiments and the model). This analysis yields a H_2-flow-dependent radiation escape factor $\theta_{10}=0.1/F^0_{H_2}$ (with the flow rate here defined in units of standard $cm^3\ s^{-1}$) and a best-fit reaction rate constant $k_{15}=3\times10^{25}/T^{1.5}\ cm^6\ mol^{-2}\ s^{-1}=8.27\times10^{-23}/T^{1.5}\ cm^6\ s^{-1}$ (with T in K).

The model, although combining several processes into the simplified representation of Eq. (15), must distinguish whether the energy of the reaction is liberated as heat or as radiation that reduces the energy content of the plasma. High-lying electronic energy levels of Ar are closely spaced, and collisional processes can thus readily remove energy as heat, but lower down the electronic state manifold (below 12.9 eV), removal of the larger quanta of energy that separate very widely spaced energy levels is much more effective by radiative loss.[32] These effects are incorporated in the model by including two rate constants that sum to k_{15}, the faster of which describes the direct radiative loss of energy to form ground-state Ar, and the smaller of which corresponds to loss of an energy corresponding to the ionization energy of Ar as heat. The ratio of the rate constant for radiative loss to the sum of the two rates (i.e., k_{15}) given in Table I is equivalent to the ratio of the energy of the lowest level in the region of a high density of electronic states (12.9 eV) to the ionization energy (15.76 eV), so that the energy stored in Ar^+ is appropriately partitioned between radiative loss (12.9 eV) and heating of the plasma (2.86 eV). Such a partitioning must be plasma-condition dependent, but has been invoked previously in studies of optical discharges[33] and an expanding plasma jet.[32] We note that, under the present experimental conditions, the net three-body recombination rate of Ar^+ we employ is several orders of magnitude smaller than the theoretical predictions of Biberman *et al.*,[34] because of fast, stepwise reionization processes.

C. Expansion of the plasma from the nozzle and gas recirculation in the reactor chamber

Given knowledge of the plasma conditions at NZRC, and the chemical kinetic reaction mechanism described above, we are now equipped to model the plume expansion into the reactor. The conservation equations[35] for mass, species, energy, and radial and axial momentum were numerically integrated, simultaneously, using thermal and caloric equations of state and initial and boundary conditions in 2D, i.e., the cylindrical (r,z), coordinate space. The explicit conservative numerical integration scheme employed a time step of 20 ns and a grid size of 0.5 mm in r and 2 mm in z, and continued until steady-state conditions were attained. The reactor chamber is approximated as two cylinders in series, with respective radii of 19 and 72.5 mm and lengths of 82 and 92 mm (cf. Fig. 1). The center of the substrate is located at ($r=0, z=155$ mm), and is a disc with a radius of 13 mm. Thermochemical data for the dominant neutral species were taken from the GRI-Mech mechanism.[36] Power-law temperature dependencies, as approximations of tabular data,[37] are used for the argon viscosity, $\mu[g/(cm\ s)]=5\times10^{-6}\ T^{0.67}$, and Ar/H thermal conductivity, $\lambda[erg/(cm\ s\ K)]=22.9T^{0.67}\times(1+5.3X_H)$.

The model output includes spatial distributions of T_{gas}, the flow field, and the number densities of the various species as a function of parameters such as the H_2 flow rate and the input power. For orientation, Fig. 4 shows 2D (r,z) plots of the calculated T_{gas} and flow field for the base Ar/H_2 plasma used in our previous diamond CVD studies (i.e., $F^0_{H_2}=1.8$ slm and $F^0_{Ar}=11.4$ slm flowing through the N torch, with a further $F^0_{Ar}=0.75$ slm into the P torch) and a total power $W=4450$ W coupled into the N-torch plasma. The hot central core of the jet is strikingly evident in the former, as are a local minimum at small z and the rapid temperature rise within ~1 cm of the substrate. The arrow lengths in the flow field plot are merely indicative of, and not directly proportional to, the absolute velocities. Nonetheless, this plot clearly illustrates the directed flow from the nozzle to the substrate and the importance of gas recirculation through the main body of the chamber and back into the narrower bore section. Such recirculation is crucial for efficient processing of hydrocarbon gases injected into the reactor when used for diamond CVD, because the annulus through which hydrocarbon process gas is injected is located within the recirculation vortex.

Figures 5(a) and 5(b) show representative data for the eight species included in the chemical kinetic model [H_2, H($n=1$), H($n=2$), H($n=3$), Ar, Ar^+, ArH^+, and e—see Table I), as well as T_{gas}, for two $F^0_{H_2}$ values—0.5 (a) and 1.0 slm (b), plotted as a function of z along the center line of the plume (i.e., $r=0$). Both plots show a clear localized minimum in T_{gas} just before the shock front at $z\sim6$ mm, in excellent accord with expectations from gas-dynamics theory,[36,38] and a dramatic increase in T_{gas} close to the substrate surface. However, the z dependence of T_{gas} in the free-plume region is seen to be $F^0_{H_2}$ dependent, increasing monotonically from ~2400 to 3100 K in the case of $F^0_{H_2}=1.0$ slm, but showing little variation with z in the case of $F^0_{H_2}=0.5$ slm. The number densities of all of the less abundant species also show greater sensitivity to z in the case of $F^0_{H_2}=1.0$ slm. These differences, which are exacerbated by focusing on number densities along the $r=0$ axis, are all attributable to reactions (11) and (12) which result in the progressive consumption of Ar^+ and formation of ArH^+ with increasing z [by reaction (11)]. ArH^+ is also destroyed in process (12), leading to an increase in electronically excited H atoms. As Fig. 5(b) nicely illustrates, the plasma is quasineutral: N_e tracks the sum $N_{Ar^+}+N_{ArH^+}$. Typical values of the Debye radius under these conditions are $\sim10^{-5}-10^{-4}$ cm.

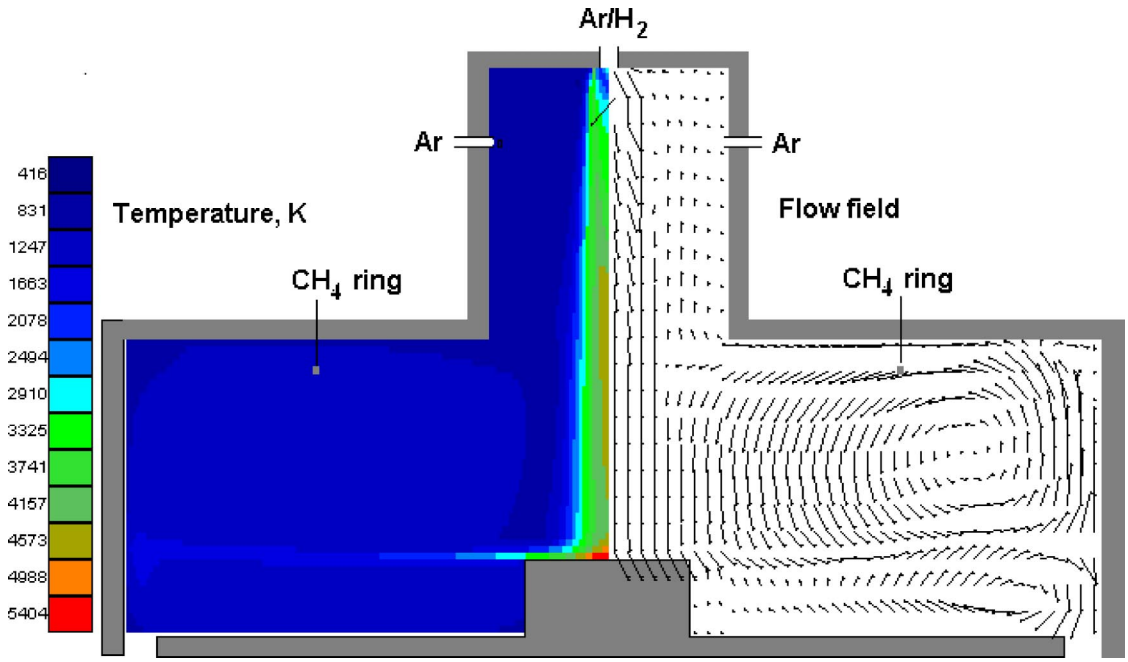

FIG. 4. (Color online) T_{gas} and flow fields for "base" plasma conditions ($F^0_{Ar}=11.4$ slm and $F^0_{H_2}=1.8$ slm flowing into the N torch, with a further $F^0_{Ar}=0.75$ slm into the P torch), with $W=4450$ W coupled into the N-torch plasma.

One-dimensional (1D) plots such as these provide a wealth of detailed information, but any full appreciation of the plume structure requires information on the r dependencies also. The $F^0_{H_2}=0.5$ slm plume, for example, which appeared rather uninteresting when viewed as a $z(r=0)$ plot, shows striking radial inhomogeneities. Figure 5(c) shows the predicted r (at $z=140$ mm) variation of T_{gas} and all species number densities bar the most abundant N_{Ar} (which increases from $\sim 1.4\times 10^{17}$ to $\sim 4.5\times 10^{17}$ cm^{-3} in line with the calculated fall in T_{gas}), and serves to clarify the function of process (11). The Ar^+ density issuing at NZRC remains concentrated on the $r=0$ axis, whereas N_{H_2} is maximal in the cooler off-axis regions where H_2 builds up through three-body recombination processes during gas recirculation in the reactor. Reaction (11) thus depletes Ar^+ progressively from the outer edge of the plume. If $F^0_{H_2}$ is sufficiently low, reactions (11) and (12) will be concentrated at the periphery of the plume, N_{ArH+}, $N_{H(n=3)}$, and $N_{H(n=2)}$ will all maximize at $r>0$ (giving the brightest emission at the edges of the plume), and N_{Ar+} will show little or no depletion along the $z(r=0)$ axis. Such is the case for the $F^0_{H_2}=0.5$ slm data shown in Figs. 5(a) and 5(c). With increasing $F^0_{H_2}$, the effects of reaction (11) and (12) will progressively reach through to the $r=0$ axis within the viewing zone and, as Fig. 5(b) shows, N_{Ar+} will drop, N_{H_2} will increase [since its major loss mechanism, reaction (11), is no longer effective], and the $H(n=2)$ and $H(n=3)$ number densities will maximize on axis and at a progressively smaller z—in good accord with the OES observations described earlier, which show retraction of the H-atom emission as $F^0_{H_2}$ increases.

The four panels in Fig. 6, which show calculated $z(r=0)$ and $z(r=4$ mm) profiles of, respectively, N_{Ar+}, N_{ArH+}, $N_{H(n=2)}$, and $N_{H(n=3)}$ for $F^0_{H_2}$ values of 0.5, 1.0, and 1.5 slm, provide further illustrations of these trends. Figure 6(a) confirms that the on-axis value of N_{Ar+} exceeds the value at $r=4$ mm at each $F^0_{H_2}$, but also shows that increases in the H_2 flow rate leads to a progressive decrease in both the width r and the length z of the Ar^+-rich part of the plume. Such trends are entirely understandable in terms of reaction (11), as are the consequent increases in N_{ArH+}. As Fig. 6(b) shows, at small z, N_{ArH+} maximizes at $r>0$, but the $r=0$ value of N_{ArH+} increases with increasing z—most evidently at the highest $F^0_{H_2}$. The $z(r=0)$ profiles of N_{ArH+} in the case of $F^0_{H_2}=1.0$ and 1.5 slm are predicted to peak at $z\sim 135$ and ~ 100 mm; the respective turn overs reflect the terminal decline in the Ar^+ ion population at large z at the higher $F^0_{H_2}$ flow rates. Electronically excited H atoms result from the dissociative recombination of ArH^+ ions and electrons [process (12)]. The $N_{H(n=2)}$ and $N_{H(n=3)}$ profiles [Figs. 6(c) and 6(d)] thus reflect the calculated trends in N_{ArH+}, modulated by the z, r dependence of N_e (which has the same form as $N_{Ar+}+N_{ArH+}$, and thus declines with increasing z and r, most notably at high $F^0_{H_2}$).

IV. RESULTS OF THE EXPERIMENTAL MEASUREMENTS

Optical emission data of the type shown in Fig. 2 provide qualitative tests of the performance of the model, which does indeed, as discussed in the preceding section, reproduce the changes in the spatial distribution of emission intensity. Quantitative tests of the model are, however, much more critical and are provided here through CRDS measurements that give absolute $H(n=2)$ column densities and information on the electron density. We first describe how these densities are extracted from experimental spectra, and then discuss the limitations of the data inversion and how quantitative comparisons with the model predictions are best made. The elec-

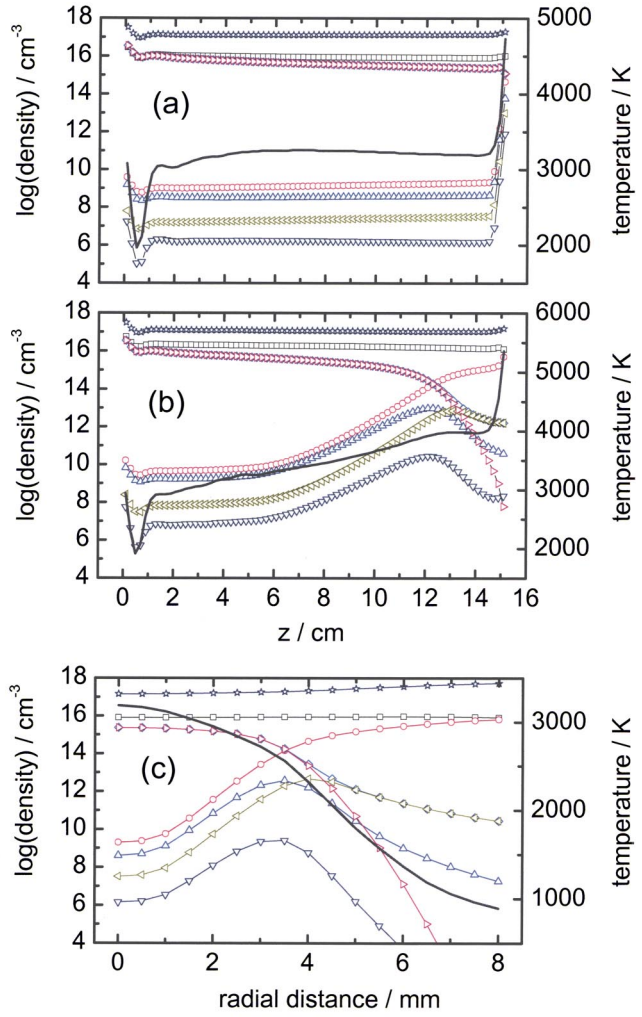

FIG. 5. (Color online) Plots showing the calculated $z(r=0)$ dependence of T_{gas} (—); and the number densities of the eight species included in the chemical kinetic model [i.e., H_2 (red ○), H($n=1$) (black □), H($n=2$) (blue △), H($n=3$) (violet ▽), Ar (violet ⋆), Ar^+ (cerise ▷), ArH^+ (khaki ◁), and electrons (turquoise ◇)] for input flows in the N torch of (a) $F^0_{H_2}=0.5$ slm, $F^0_{Ar}=13$ slm and (b) $F^0_{H_2}=1$ slm, $F^0_{Ar}=12.5$ slm. (c) shows the calculated $r(z=140$ mm) dependencies of all of the corresponding quantities bar N_{Ar}, for the case of $F^0_{H_2}=0.5$ slm. Conditions at NZRC in the model are the following: $P=938$ Torr, $T=12\,100$ K, $X_e=0.105\,5$ for (a) and (b), and $X_H=0.064\,6$, $v=2246$ m s^{-1} (a); $X_H=0.123$, $v=2330$ m s^{-1} (b).

tron density is an important plasma parameter, but precise measurements are challenging: under conditions of high electron density, interferometric methods[39] or Thomson scattering[11,40] can be used. At the relatively low electron densities of the arc jet reactor plume, however, we instead retrieve electron densities from the Stark broadening of atomic absorption lines.

Absorption measurements are made using the Balmer-β transition: the choice of a transition within the Balmer series is dictated in part by the experimental convenience of the visible wavelength region, and because H-atom-containing plasmas rapidly become optically thick to Lyman series radiation.[41] Measurements obtained using the H Balmer-β line can be directly compared with the outcomes of the model of the arc jet because the chemical kinetic scheme treats H($n=1$) and H($n=2$) independently. The $n=2$ level is optically coupled to the ground state through emission of

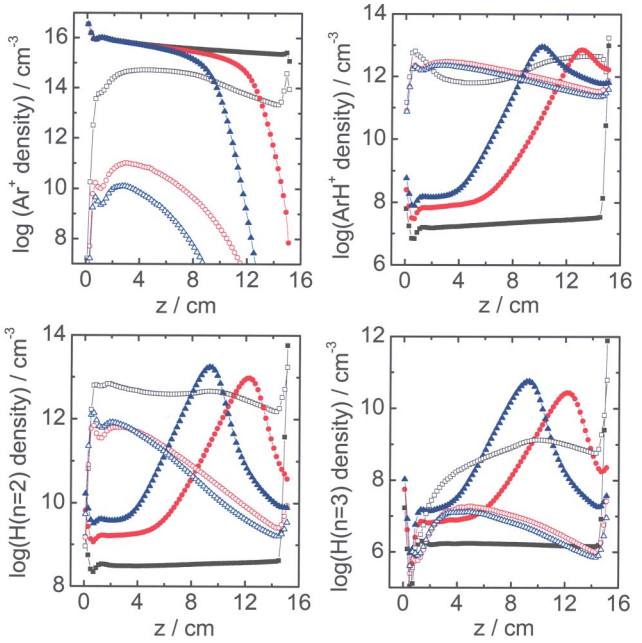

FIG. 6. (Color online) Calculated variations of the number densities of Ar^+, ArH^+, H($n=2$), and H($n=3$) with distance z from the nozzle, for two different radial distances r. Closed symbols are for $r=0$ and open symbols are for $r=4$ mm. The different shapes denote the flow rates of H_2, $F^0_{H_2}=0.5$ slm (black squares); $F^0_{H_2}=1.0$ slm (red circles); and $F^0_{H_2}=1.5$ slm (blue triangles).

Lyman-α radiation (10), but, because of the very high Lyman-α oscillator strength, this radiation is effectively trapped by reabsorption in the plasma.[42] The metastable $2s^2S_{1/2}$ level is strongly coupled to the radiative $2p^2P_{1/2,3/2}$ levels by a combination of Stark mixing and collision with heavy particles (Ar, H_2).[43] Interconversion between the various levels is thus rapid, leading to a statistical distribution of populations.

A. H($n=2$) density

CRDS involves the measurement of the rate of loss of intensity experienced by a laser passing through a ring-down cavity. The loss rate coefficient κ is the reciprocal of the ring-down time τ and is given by[25]

$$\kappa = \frac{1}{\tau} = \frac{c(1-R+n\sigma d)}{L}, \tag{16}$$

where c is the speed of light, R is the reflectivity of the mirrors forming the cavity of length L, and σ and d are the cross section of, and path length through, the absorbing species, respectively. A particular cavity will have a characteristic "empty" ring-down rate, $\kappa=1/\tau_0$, due to losses at the mirrors; here, however, this is subtracted from the measured signal, and the resultant change in the ring-down rate, $\Delta\kappa$, is determined simply by H($n=2$) absorption losses.

The integral over the laser frequency of the absorption coefficient α is directly related to the number density of absorbers, $N_{H(n=2)}$, by the frequency-integrated absorption cross section. If the absorber is uniformly distributed over a region

of length d along the absorption measurement direction, it follows that the measured change in ring-down rate is proportional to the absorption coefficient

$$\int \alpha \mathrm{d}\nu = N_{\mathrm{H}(n=2)} \int \sigma \mathrm{d}\nu = \frac{1}{c}\frac{L}{d} \int \Delta\kappa \mathrm{d}\nu. \tag{17}$$

Within the Balmer-β absorption feature, there are seven allowed transitions, each having its own frequency and absorption cross section. In our spectra, the combination of Doppler and Stark broadening means that the individual, closely spaced transitions are not resolved, so our measured peak is related to some "average" absorption cross section. Using the assumption that the population distribution in the $n=2$ level is statistical, we can calculate the rates of depopulation (by absorption) of each of the three H($n=2$) levels ($^2S_{1/2}$, $^2P_{1/2}$, and $^2P_{3/2}$), and sum these rates with weightings determined by the ratio of the level degeneracy to the total degeneracy [$g_{\mathrm{H}(n=2)}=8$]. The National Institute of Standards and Technology (NIST) database[44] lists Einstein A-coefficients for the seven transitions, and for an absorption from level j to level k at wavelength λ_{jk} (in units of cm), the A_{jk} coefficients relate to absorption cross sections, σ_{jk}, via

$$\int \sigma_{jk} d\nu = \frac{1}{8\pi} A_{jk} \lambda_{jk}^2 \frac{g_k}{g_j}, \tag{18}$$

with integration across the full frequency range of the absorption profile. The weighted sum over the seven transitions gives the following expression for the average absorption cross section, integrated over the Balmer-β absorption feature

$$\int \sigma d\nu = \frac{1}{64\pi} \sum_{j,k} A_{jk} \lambda_{jk}^2 g_k, \tag{19}$$

with a resultant value of 3.1684×10^{-3} cm^2 s^{-1}. Thus, the column density (the integrated line-of-sight concentration) of H($n=2$), denoted as $D_{\mathrm{H}(n=2)}$, is calculated from

$$D_{\mathrm{H}(n=2)}[\mathrm{cm}^{-2}] = \frac{L}{c} \frac{\int \Delta\kappa \mathrm{d}\nu}{3.1684 \times 10^{-3}}. \tag{20}$$

The results are derived as column densities because, as revealed by the model, the H atoms are not distributed homogeneously throughout the plasma, so an accurate estimate of the absorber path length d is not possible.

Absorption spectra recorded under four different hydrogen flows and at $z=140$ mm are shown in Fig. 7. Considerable care was taken to minimize flattening of the tops of the peaks because of strong absorption at line center, which causes the ring-down decay trace to decay rapidly to zero, leaving only a small time region that can be fitted. Some residual loss of absorption at line center remains, but the flanks can be fitted to yield all the required parameters. The effects of laser-pulse energy were also investigated to check for, and avoid, saturation effects. With the H_2 flow rate maintained at 300 sccm, cavity ring-down (CRD) spectra were recorded over a range of laser-pulse energies from 0.15–1.7 mJ, as measured at the output of the dye laser, and

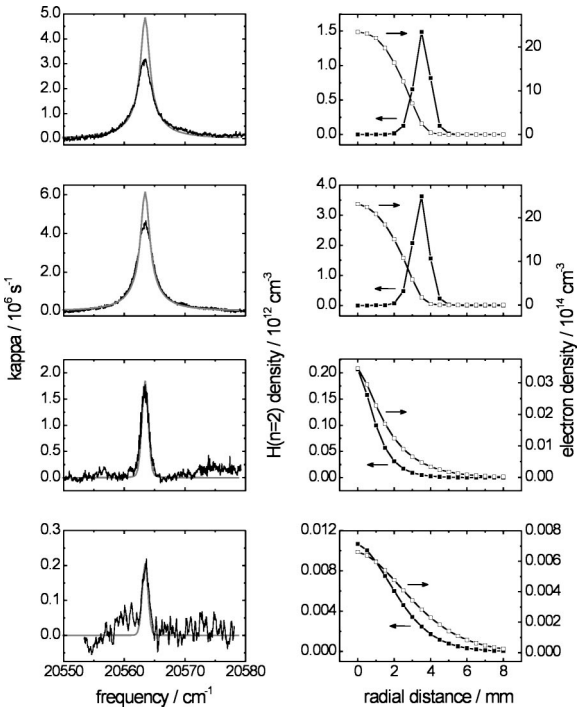

FIG. 7. The left-hand column shows experimental CRDS measurements (in black) of H Balmer-β lines in absorption at four different flow rates of H_2: from top to bottom these are $F^0_{\mathrm{H}_2}=0.2$, 0.5, 1.0, and 1.5 slm. Also shown overlaid (in grey) are simulations of the absorption features carried out using data from the model calculations of spatially resolved H($n=2$) number densities (■) and electron densities (□), as plotted in the right-hand column. For clearer comparison with the experimental data, the simulated profiles have been scaled vertically by factors of ×2, ×1, ×1.5, and ×1.5 for respective H_2 flows of $F^0_{\mathrm{H}_2}=0.2$, 0.5, 1.0, and 1.5 slm.

the sides and wings of the profiles fitted to single Lorentzian functions. Note that the intracavity pulse energy will be much reduced from the energies quoted here because of the high reflectivity of the cavity input mirror and imperfect matching of the laser pulse to cavity modes. The areas of the fit functions were analyzed according to the procedure outlined above, and, together with the linewidths, were found to be independent of the laser energy. The calculated hydrogen atom column density and electron number density (*vide infra*) will thus also be independent of the laser power within the tested range. If we were in a saturation regime, the measurements would show a decrease as a function of laser power. All further spectra reported here were obtained using a laser power of 1 mJ/pulse as measured at the dye laser exit.

From the areas under the fits to the peaks, corresponding to the integral of $\Delta\kappa$ over the absorption profile, and using the data reduction procedure outlined earlier, the column densities of H($n=2$) were calculated for different added flows of H_2. The results are shown in Fig. 8, together with the column densities predicted by the model. Qualitatively, the observed and predicted variations of column densities with added flow of H_2 are in excellent accord, and the degree of quantitative agreement is also impressive: the model and measurements agree to within a factor of 2. As is evident in the bottom panel of Fig. 7, the H($n=2$) absorption is weak at

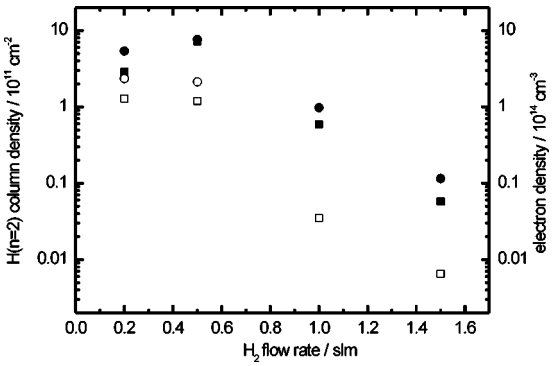

FIG. 8. A comparison of the model and experimental H($n=2$) column densities and electron densities (see details of how these values are derived). The data shown are H($n=2$) from the model (■) and experimental measurements (●), and model (□) and measured (○) electron densities. In the constructed absorption profiles at 1.0- and 1.5-slm H_2 (shown in Fig. 7), no significant Lorentzian contribution can be observed, and thus experimental electron densities are not plotted for these $F^0_{H_2}$.

the highest H_2 flow rate ($F^0_{H_2}=1.5$ slm) and the measured Balmer-β absorption is thus subject to some errors resulting from the signal-to-noise ratio.

The sharp, order-of-magnitude fall in the H($n=2$) column density at $z=140$ mm with increasing H_2 flow rate from $F^0_{H_2}=0.5-1$ slm is a consequence of the depletion of Ar^+ ions by reaction with H_2, thus reducing the production of ArH^+, which is the source of electronically excited H atoms [via (12)]. The H_2 flow-rate range, for a fixed z, at which this falloff is predicted to occur depends strongly on the quality of the kinetic data in the reaction scheme used in the model calculations. It is clear from Fig. 8 that the model is capturing well the essential features of the experimental observations.

B. Electron density

The right-hand panels of Fig. 7 show the calculated radial distributions of the electron and H($n=2$) number densities at $z=140$ mm, under the conditions of flow of H_2 used in the experimental measurements of the adjacent H Balmer-β spectra. It is evident from the calculations that the spatial distributions of H($n=2$) atoms and electrons are very different at low flow rates of H_2 ($\leqslant 0.5$ slm). The density of the electrons is calculated to maximize in the center of the plasma expansion, whereas, for reasons discussed in Sec. III C, the H($n=2$) distribution peaks in a ring around the center axis. At greater H_2 flow rates, the electron density is calculated to fall off markedly; the H($n=2$) density also declines in magnitude and retracts to peak at $r=0$. Direct excitation of H atoms by electron impact is not important in the expanded plasma at typical temperatures of 2000–4000 K, and the main source of H($n>1$) atoms is via the dissociative ion-electron recombination processes (11) and (12). The H($n>1$) production rate is thus proportional to the product of the Ar^+, H_2, and electron number densities. These exhibit different, nonuniform spatial distributions, which clearly depend upon the reactor parameters; complex and variable H($n>1$) spatial profiles result. The electron density manifests itself in the experimental measurements through Stark broadening of the Balmer-β absorption feature, and spectral linewidths thus depend on the electron density in close proximity to the maxima of the H($n=2$) atom densities along the viewed column. As a result, Stark-broadening measurements in the arc jet plume risk underestimation of the peak electron density at low H_2 flow rates, if interpreted without the benefit of guidance from the model. The most useful test of the model predictions comes from a simulation of the experimental line profiles using the computed electron and H($n=2$) density distributions. At the higher flow rates, the electron density has declined to such an extent that the Stark effect contributes less to the linewidths than Doppler broadening, and under such circumstances, reliable electron densities cannot be extracted from the spectra.

To simulate Balmer-β line profiles, we used the modeled temperature and electron and H($n=2$) density information for each radial cell (at $z=140$ mm) to compute contributions to the overall wave-number-dependent absorption. Voigt profiles for each radial cell were calculated as a convolution of a Gaussian, Doppler-broadened H($n=2$) absorption line and a Lorentzian profile, normalized to unit area, with width determined by the r-dependent electron density. The full-width-at-half-maximum intensity (FWHM) of the Gaussian function depends on the cell temperature T according to

$$\Delta_D = 7.16 \times 10^{-7} \overline{\nu} \sqrt{\frac{T}{m}}, \tag{21}$$

with $\overline{\nu}$ as the line center wavenumber (in cm^{-1}) and m as the molar mass (in $g\,mol^{-1}$) of the absorber. The area of the Gaussian function is determined by the number density of H($n=2$) and the average line-integrated absorption cross section (as described in the preceding section). The homogeneous Stark-broadening mechanism contributes a Lorentzian line shape with FWHM (in cm^{-1}) given by

$$\Delta_L = 5 \times 10^{-9} \alpha_{1/2} N_e^{1/3} \frac{1}{\lambda^2}, \tag{22}$$

with λ in units of cm and N_e in units of cm^{-3}. The half-width parameter $\alpha_{1/2}$ for the Balmer-β line was obtained from Ref. 45; the value of 0.079 we use does not change more than 10% over our parameter range. The resulting Voigt profiles for each grid point were then summed to yield the $F^0_{H_2}$-dependent line shapes, plotted with the experimental data in Fig. 7. For better appraisal of the calculated widths, the areas of the calculated peaks have been multiplied by the ratios of the measured to calculated areas.

Under conditions of low hydrogen flow, the flanks of the calculated curves (largely determined by the Lorentzian contribution to the line shape) agree very well with the measured profiles, a strong indication that the calculated density distributions for electrons and H($n=2$) reflect accurately the distributions in the arc jet plume. At high hydrogen flow, the electron densities are too low to have an effect, and the simulated peak profiles are mostly Gaussian in character, again in good correspondence with the experimental determinations.

Radially averaged electron densities, weighted by the H($n=2$) radial number density distributions, can also be derived from the model at $z=140$ mm for the different $F^0_{H_2}$

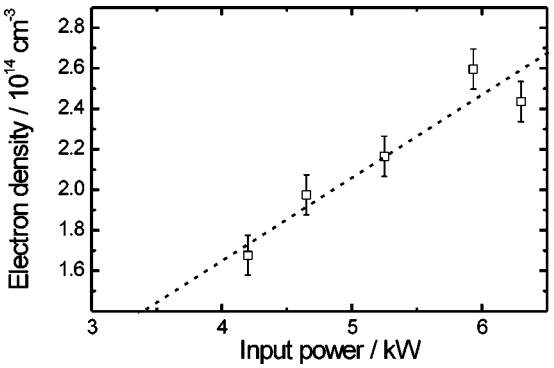

FIG. 9. The variation of electron density as determined by measurement of the Stark broadening of the Balmer-β line by CRDS, with power delivered to the arc jet, W_0. The dashed line shows a linear fit through the data and the origin.

conditions using the following procedure. At $z=140$ mm, for each radial point across the plume diameter for which the model generates values of N_e, the H($n=2$) number density, and T_g, a Voigt profile was calculated using a Lorentzian component with FWHM calculated from Eq. (22) and a Gaussian component with FWHM from Eq. (21). The areas of the Voigt profiles were scaled according to the ratios of H($n=2$) number densities, and the profiles then summed to produce a composite profile that mimics the experimental measurement. The composite profiles for $F^0_{H_2}=200$ and 500 sccm were each then fitted to a single Voigt function, and the radially averaged electron density deduced from the FWHM. At higher H_2 flow rates, the Lorentzian contribution to the linewidth was negligible. In Fig. 8, these values are compared with the equivalent densities extracted from single Voigt function fits to the experimental line profiles. The Stark-broadening measurements are reproduced quantitatively by the model, and the onset of a sharp decline in the electron density with increasing $F^0_{H_2}$ in the region of 0.5 slm is evident in both data sets.

C. Plasma power dependence

To study the effects of the input power on the electron density, CRD spectra of the H Balmer-β absorption were recorded as a function of total input power to the reactor (W_0) at a hydrogen flow rate of $F^0_{H_2}\sim 0.5$ slm, with the results shown in Fig. 9. The error bars are determined from three spectral profiles recorded during the measurement series at a total input power to the reactor of 5.2 kW. The dotted line is a linear fit to the data. The observed correlation between the input power and N_e at $z=140$ mm suggests that the measured N_e this far downstream of the nozzle could be representative of the extent of free-electron production in the torch. Model calculations reproduce near quantitatively the variation of this downstream electron density, but this direct connection is not, *a priori*, to be expected because of the complexity of the neutral and ionic plasma chemistry in the jet. In fact, the model calculations show that these particular measurements should not be characteristic of electron production in the torch. Figure 10 displays the calculated dependence of X_e and the temperature at the output of the nozzle, NZRC, on the power delivered to the inlet plasma. Further calculations were performed for two different input powers, with corresponding inlet temperatures $T=11\,300$ and 12 100 K and respective electron mole fractions $X_e=0.0655$ and 0.1055. Recalling that our measurements of H Balmer-β absorption characterize the electron density in an annular region displaced from the central axis, and centered around $r\sim 3.5$ mm, the axial behaviors of the electron densities at $r=0$ and $r=3.5$ mm are compared in Fig. 11 for the two input powers. The $\sim$50% difference in the peak electron densities at the inlet nozzle ($z=0$) is reduced to $\sim$10% within the first 40 mm of the gas expansion. The density of the main cationic species, Ar^+ is approximately equal to N_e in this region, and thus the three-body recombination processes that remove electrons have rates that are proportional to $(N_e)^3$. All downstream electron densities (for $z>40$ mm) are thus not strongly influenced by the inlet N_e values, and this is especially true for the electron densities away from the plume axis, such as at $r=3.5$ mm. The correlation observed in the CRDS measurements at $z=140$ mm, and confirmed by calculations, is thus no more than a coincidence resulting from a combination of the complicated plasma chemical and transport processes in the arc jet plume.

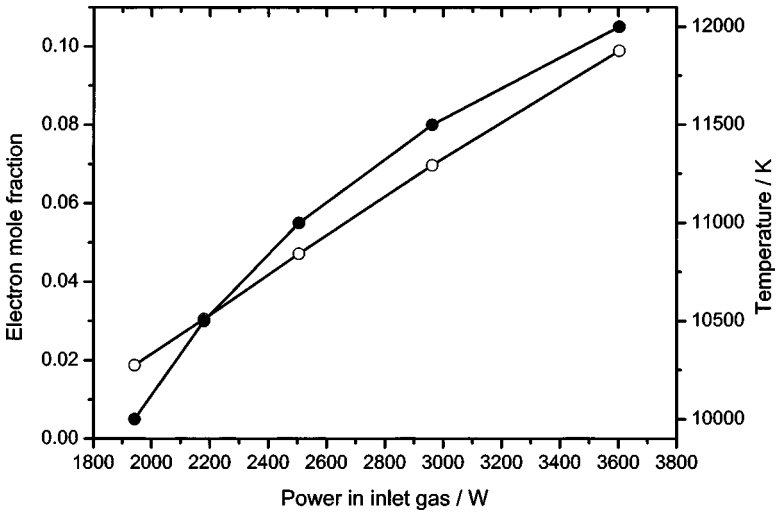

FIG. 10. Computed electron mole fractions (○ and left-hand axis) and temperatures (● and right-hand axis) at the nozzle inlet, NZRC, as function of the power to the inlet equilibrium plasma.

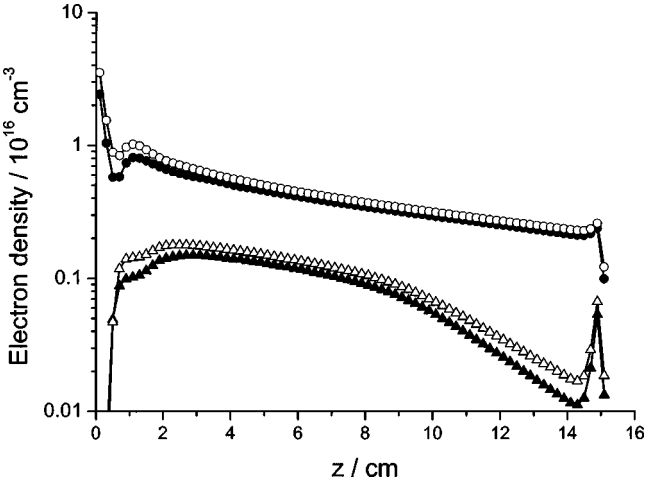

FIG. 11. Calculated axial behavior of electron densities at $r=0$ (circles) and $r=3.5$ mm (triangles) for different inlet ionization degrees with $X_e=0.065\,5$ (open symbols) and corresponding temperatures $T=11\,300$ and 12 100 K.

V. CONCLUSIONS

Key properties of the base Ar/H_2 plasma within a $\leqslant$10-kW, twin-nozzle dc arc jet reactor have been characterized successfully by computer modeling that has, itself, been validated by a range of experimental measurements. The model contains an accurate description of the initial conditions in the primary plasma torch head, derived from straightforward measurements of the physical dimensions of the torch nozzle and the amount of supplied power that is coupled into the Ar/H_2 mixture. Optical emission imaging of the plume defines the ranges of input gas flows, F^0_{Ar} and F^0_H, of interest for the modeling studies. With initial gas flows of $F^0_{Ar}=11.4$ slm and $F^0_{H_2}=1.8$ slm in the N torch, a further $F^0_{Ar}=0.75$ slm into the P torch, and 4450 W coupled into the N-torch plasma, the gas temperature, pressure, and velocity in the throat of the nozzle NZRC are $T=12\,100$ K, $P=914$ Torr, and $v=2450$ m s^{-1}. Expansion of this mixture into a lower pressure reactor chamber generates a cylindrical plume of activated gas, treated in 2D in the model, composed mostly of Ar, Ar^+, H, ArH^+, and free electrons. Subsequent reactions, summarized in a reduced chemical scheme (eight distinct chemical species and 20 reactions), form H_2 and electronically excited atoms including $H(n=2)$ and $H(n=3)$ that radiate photons, giving the plume its characteristic intense emission. The contraction of this emission away from the periphery of the cylindrical plume, towards the center ($r=0$) axis, and then back towards the torch head with increasing flow of H_2 is well described by the model calculations of spatial distributions of $H(n>1)$. Computed $H(n=2)$ number densities are compared with CRDS measurements of $H(n=2)$ absorption via the Balmer-β transition at $z=140$ mm and are in near-quantitative agreement, successfully capturing the trend of decreasing $H(n=2)$ with increased H_2 flow to the primary torch. Stark broadening of the H Balmer-β transition depends upon the local electron density in close proximity to the maximum in the $H(n=2)$ atom distribution; the model demonstrates that at low flow rates of H_2, the distributions of electrons and excited H atoms peak in different radial regions of the plume, and thus direct analysis of the Stark broadening would underestimate the peak electron density. The most useful comparisons come from simulations of the CRDS data using computed distribution functions, and agreement is excellent. Care must thus be taken in using Stark-broadening measurements to deduce electron densities when the electrons and H atoms are inhomogeneously distributed, with densities peaking in spatially separated regions of the plasma.

The intercomparison of quantitative experimental data with the predictions of the computer model has proven essential for the successful development of a numerical treatment of the arc jet plasma. The refined model for the base plasma generated in the Ar/H_2 mixture underpins the more chemically complicated model of the arc jet when methane is added in order to grow thin diamond films by CVD. The kinetic scheme described herein is successful in describing many disparate observations, including electron and $H(n=2)$ number densities, spatial distributions of Balmer-α optical emission from the plume, the variation of these quantities with added flow of H_2 and, when CH_4 is present, absolute column densities and temperatures of radicals such as C_2 and CH. Some limitations of the model do, however, remain. The representation of the reabsorption of the radiation emitted within the plume is relatively crude, as is the reduced treatment of the multistep recombination of Ar^+ with an electron. The net recombination rate for $Ar+e+e$ is three to four orders of magnitude less than the value predicted by theoretical models (at lower T)—a requirement also invoked by others to interpret their data[9,34,38]—but the temperature dependence employed here differs from the $T^{4.5}$ behavior used in other studies.

ACKNOWLEDGMENTS

The authors are most grateful to EPSRC, for funding via the portfolio award LASER; to Element Six Ltd. (formerly De Beers Industrial Diamonds) for the long-term loan of the dc-arc plasma jet system; to Bristol colleagues K. N. Rosser, for his numerous contributions to the work described herein, and Jie Ma, for his critical reading of an earlier version of this manuscript; to the Royal Society, for a Joint Project Grant that enables the Bristol-Moscow collaboration; to NATO (MNRA, AJOE) and the Russian Education and Science Ministry (YAM) for the award of a NATO-Russia collaborative grant (Grant No. JSTC.RCLG.979556); and to RFBR for Key Science Schools Grant No. 1713.2003.2 (YAM). R.E. thanks the "Stichting voor Fundamental Onderzoek der Materie (FOM)" for financial support.

[1] R. F. G. Meulenbroeks, A. J. van Beek, A. J. G. van Helvoort, M. C. M. van de Sanden, and D. C. Schram, Phys. Rev. E **49**, 4397 (1994).
[2] R. F. G. Meulenbroeks, R. A. H. Engeln, M. N. A. Beurskens, R. M. J. Paffen, M. C. M. van de Sanden, J. A. M. van der Muller, and D. C. Schram, Plasma Sources Sci. Technol. **4**, 74 (1995).
[3] M. J. de Graaf, R. Severens, R. P. Dahiya, M. C. M. van de Sanden, and D. C. Schram, Phys. Rev. E **48**, 2098 (1998).
[4] N. Singh, M. Razafinimanana, and A. Gleizes, J. Phys. D **31**, 2921 (1998).
[5] A. Bogaerts and R. Gijbels, J. Anal. At. Spectrom. **15**, 441 (2000).
[6] S. Mazouffre, M. G. H. Boogaarts, I. S. J. Bakker, P. Vankan, R. Engeln, and D. C. Schram, Phys. Rev. E **64**, 016411 (2001).
[7] V. Sember, D. V. Gravelle, and M. I. Boulos, J. Phys. D **35**, 1350 (2002).

[8]V. Rat, P. Andre, J. Aubreton, M. F. Elchinger, P. Fauchais, and A. Lefort, Plasma Chem. Plasma Process. **22**, 453 (2002).
[9]S. E. Selezneva, M. I. Boulos, K. G. Y. Letourneur, M. F. A. M. van Hest, and M. C. M. van de Sanden, Plasma Sources Sci. Technol. **12**, 107 (2003).
[10]K. T. A. L. Burm, B. Jodoin, P. Proulx, and M. I. Boulos, Plasma Sources Sci. Technol. **12**, 362 (2003).
[11]A. B. Murphy, Phys. Rev. E **69**, 016408 (2004).
[12]M. A. Cappelli and T. G. Owano, in *Low Pressure Synthetic Diamond*, edited by B. Dischler and C. Wild (Springer, Berlin, 1998), pp. 59–84.
[13]M. Vilotijevic, S. T. Dimitrijevic, and I. Randjelovic, J. Mater. Sci. Lett. **12**, 1261 (1993).
[14]W. Juchmann, J. Luque, and J. B. Jeffries, Appl. Opt. **39**, 3704 (2000), and references therein.
[15]V. G. Pereverzev, A. S. Pozharov, V. I. Konov, V. G. Ralchenko, S. Metev, and G. Sepold, Diamond Relat. Mater. **9**, 373 (2000).
[16]W. X. Pan, F. X. Lu, W. Z. Tang, G. F. Zhong, Z. Jiang, and C. K. Wu, Diamond Relat. Mater. **9**, 1682 (2000).
[17]J. A. Smith, K. N. Rosser, H. Yagi, M. I. Wallace, P. W. May, and M. N. R. Ashfold, Diamond Relat. Mater. **10**, 337 (2001).
[18]J. B. Wills, J. A. Smith, W. E. Boxford, J. M. F. Elks, M. N. R. Ashfold, and A. J. Orr-Ewing, J. Appl. Phys. **92**, 4213 (2002).
[19]Y. A. Mankelevich, N. V. Suetin, M. N. R. Ashfold, W. E. Boxford, A. J. Orr-Ewing, J. A. Smith, and J. B. Wills, Diamond Relat. Mater. **12**, 383 (2003).
[20]C. J. Rennick, A. G. Smith, J. A. Smith, J. B. Wills, A. J. Orr-Ewing, M. N. R. Ashfold, Y. A. Mankelevich, and N. V. Suetin, Diamond Relat. Mater. **13**, 561 (2004).
[21]J. Isberg, J. Hammersberg, E. Johansson, T. Wilkstrom, D. J. Twitchen, A. J. Whitehead, S. E. Coe, and G. A. Scarsbrook, Science **297**, 1670 (2002).
[22]D. G. Goodwin and J. E. Butler, in *Handbook of Industrial Diamonds and Diamond Films*, edited by M. A. Prelas, G. Popovici, and L. K. Bigelow (Marcel Dekker, New York, 1998), pp. 527–581.
[23]X. Xiao, J. Birrell, J. E. Gerbi, O. Auciello, and J. A. Carlisle, J. Appl. Phys. **96**, 2232 (2004), and references therein.
[24]C. J. Rennick, R. Engeln, J. A. Smith, A. J. Orr-Ewing, M. N. R. Ashfold, and Yu. A. Mankelevich, (unpublished).
[25]M. D. Wheeler, S. M. Newman, A. J. Orr-Ewing, and M. N. R. Ashfold, J. Chem. Soc., Faraday Trans. **94**, 337 (1998).
[26]G. Berden, R. Peeters, and G. Meijer, Int. Rev. Phys. Chem. **19**, 565 (2000).
[27]I. Labazan and S. Milošević, J. Phys. D **37**, 2975 (2004).
[28]*Physical Encyclopaedia* (Moscow, 1988), Vol. 1, p. 300.
[29]Yu. P. Raizer, *Physics of Gas Discharges* (Nayka, Moscow, 1987).
[30]F. J. Gordillo-Vázquez and J. M. Abella, Plasma Sources Sci. Technol. **11**, 498 (2002).
[31]B. Jackson and M. Persson, J. Chem. Phys. **96**, 2378 (1992).
[32]M. C. M. van de Sanden, J. M. de Reg, and D. C. Schram, Phys. Rev. E **47**, 2792 (1993).
[33]G. I. Kozlov, V. A. Kuznetso, and V. A. Masyukov, Zh. Eksp. Teor. Fiz. **66**, 954 (1974) (in Russian).
[34]L. M. Biberman, V. S. Vorob'ev, and I. T. Yakubov, *Kinetics of Non-Equilibrium Plasmas* (Plenum, New York, 1987).
[35]S. E. Selezneva, M. I. Boulos, M. C. M. van de Sanden, R. Engeln, and D. C. Schram, J. Phys. D **35**, 1362 (2002).
[36]G. P. Smith *et al.*, http://www.me.berkeley.edu/gri_mech/
[37]*Handbook of Physical Data*, edited by I. S. Grigoriev and E. Z. Meilihov (Energoatomizdat, Moscow, 1991), p. 365.
[38]D. C. Schram, S. Mazouffre, R. Engeln, and M. C. M. van de Sanden, in *Atomic and Molecular Beams*, edited by R. Campargue (Springer, New York, 2001), p. 209.
[39]C. C. Dobson and I. Hrbud, J. Appl. Phys. **96**, 94 (2004).
[40]K. Muraoka, K. Uchino, and M. D. Bowden, Plasma Phys. Controlled Fusion **40**, 1221 (1998).
[41]H. F. Dobele, U. Czarnetzki, and A. Goehlich, Plasma Sources Sci. Technol. **9**, 477 (2000).
[42]T. Holstein, Phys. Rev. **83**, 1159 (1951).
[43]S. R. Ryan, S. J. Czuchlewski, and M. V. McCusker, Phys. Rev. A **16**, 1892 (1977).
[44]J. Reader, C. H. Corliss, W. L. Wiese, and G. A. Martin, Natl. Stand. Ref. Data Ser. (U.S., Natl. Bur. Stand.) **68**, (1980).
[45]C. R. Vidal, J. Cooper, and E. W. Smith, Astrophys. J., Suppl. **37**, 214 (1973).
[46]N. Terazawa, M. Ukai, N. Kouchi, K. Kameta, and Y. Hatano, J. Chem. Phys. **99**, 1637 (1993).
[47]B. L. Preppernau, K. Pearce, A. Tserepi, E. Wurzberg, and T. A. Miller, Chem. Phys. **196**, 381 (1995).
[48]D. K. Bedford and D. Smith, Int. J. Mass Spectrom. Ion Processes **98**, 179 (1990).
[49]R. F. G. Meulenbroeks, R. A. H. Engeln, C. Box, I. De Bari, M. C. M. van de Sanden, J. A. M. van der Muller, and D. C. Schram, Phys. Plasmas **2**, 1002 (1995).